

Supporting information for “Direct Laser Writing from Aqueous Precursors for Nano to Microscale Topographical Control, Integration, and Synthesis of Nanocrystalline Mixed Metal Oxides”

Cody Kindle¹, Alexander Castonguay¹, Shannon McGee¹, John A. Tomko², Patrick E. Hopkins²⁻⁴, and Lauren D. Zarzar^{*1,5}

1. Department of Chemistry, The Pennsylvania State University, University Park, PA 16802
2. Department of Materials Science and Engineering, University of Virginia, Charlottesville, VA, 22904
3. Department of Mechanical and Aerospace Engineering, University of Virginia, Charlottesville, VA, 22904
4. Department of Physics, University of Virginia, Charlottesville, VA, 22904
5. Materials Research Institute, The Pennsylvania State University, University Park, PA 16802

*corresponding author, ldz4@psu.edu

Supporting Videos

Video S1. Mn₂O₃ is laser deposited off of a platinum line using manganese nitrate as the precursor. Bubbles generated at the reaction site rapidly detach from the surface.

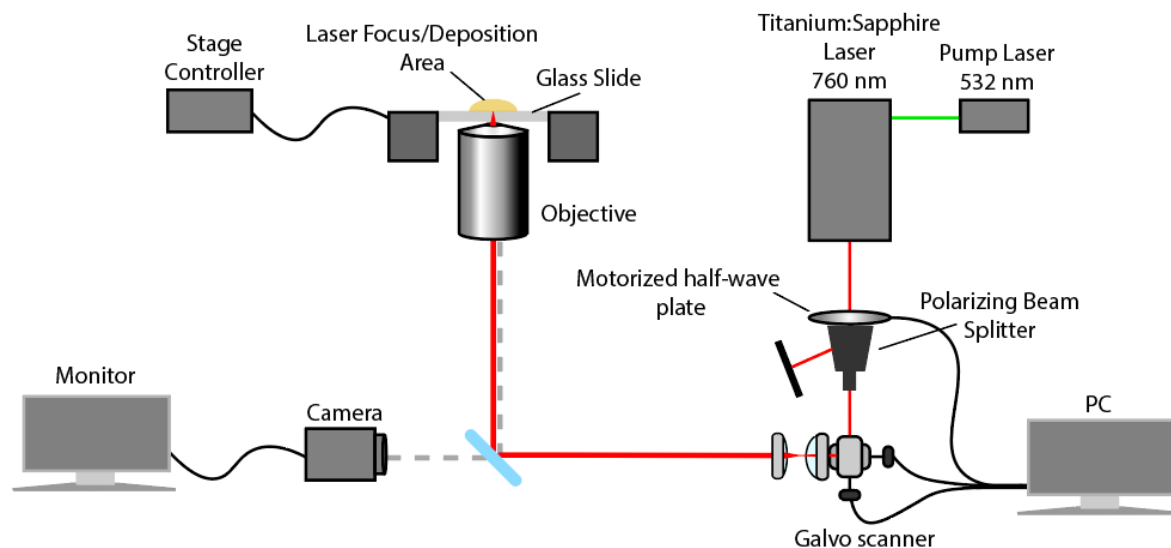
Video S2. Cr₂O₃ is laser deposited off of a platinum line using chromium nitrate as the precursor. Significant pinning and spreading of the bubble at the deposition site contributes to decreased resolution.

Chemicals

All chemicals are commercially available and used as received. Al(NO₃)₃·9H₂O reagent grade, Co(NO₃)₂·6H₂O reagent grade (Fisher Science); TiOSO₄·xH₂SO₄·yH₂O synthesis grade, Zn(NO₃)₂·6H₂O >99.0%, Na₃IrCl₆·xH₂O, Mn(NO₃)₂ 50% solution (Sigma Aldrich); VOSO₄·xH₂O 99.9%, Cr(NO₃)₃·9H₂O 98.5%, FeN₃O₉·H₂O 98.0%, FeCl₂·4H₂O 98.0%, Ni(NO₃)₂·6H₂O 98%, Y(NO₃)₃·6H₂O 99%, ZrO(NO₃)₂·xH₂O 99.95%, (NH₄)₆Mo₇O₂₄·4H₂O 99%, (NH₄)₃RhCl₆·xH₂O 99.99%, (NH₄)₂PdCl₆ 99.9%, AgNO₃ 99.9%, NH₄ReO₄ 99+%, H₈Cl₄N₂Pt 99.9%, (NH₄)AuCl₄·xH₂O 99.99%, (NH₄)₂RuCl₆ 99.99% (Alfa Aesar); Cu(NO₃)₂·6H₂O, (NH₄)₃Fe(C₂O₄)₃·3H₂O 98%, C₆H₅Na₃O₇ 98% (Acros Organics). All metal and metal oxide precursor solutions were prepared by dissolving the precursor salts in reverse osmosis water at concentrations found in Table 1 in the primary text.

Direct Laser Writing Optical Setup

All depositions employed a Coherent Mira Optima 900-F titanium:sapphire laser operating at 760 nm in either femtosecond pulse mode (for initial deposition of platinum absorber) or continuous wave (for deposition of metal and metal oxide materials). The laser output was controlled using a half wave-plate/polarizing beam-splitter pair, with the half wave-plate controlled by a motorized rotation mount (Thorlabs K10CR1) which allowed for continuous tuning of the laser power during deposition. The laser focus was translated using a galvo scanner (Nutfield open frame head XLR8 – 10 mm clear aperture), which allowed oscillation of the laser spot as it entered a microscope objective (air 40x Nikon Plan Fluor objective with 0.60 NA, or a 60x Nikon Plan Fluor oil immersion objective with 1.4 NA) situated on an inverted microscope (ASI automated RAMM/modular infinity microscope system with motorized stage). Lenses were used to collimate and expand the beam to fill the back of the microscope objective. Laser powers reported were measured at the back of the objective. A schematic of the laser writing setup is below.



Scheme S1. Schematic representation of the direct laser writing optical setup, as described in detail in the Supporting Information section “Direct Laser Writing Optical Setup”.

Material Deposition

The initial optical absorber typically used was platinum, deposited onto a borosilicate glass coverslip using a multiphoton reduction process as described elsewhere¹. The platinum precursor was then washed off, and a new precursor was placed on the coverslip. The laser was focused through a microscope objective onto the platinum absorber to create the laser induced thermal voxel, thereby depositing material directly from the precursor fluid. Patterns were “drawn” with the laser by both scanning the laser and translating the microscope stage. To switch materials, the precursor fluid was rinsed off and replaced. In order to deposit materials in layers, the laser was rastered over the bottom-layer material with an increased power to promote the deposition of the second material on top. This could be repeated for multiple layers.

Annealing

The iron oxide sample in Figure 2 was annealed using a Thermolyne 48000 furnace with a ramp rate of 10 °C/min to 450 °C for 4 hours with a cool down rate of 1°C/min. The sample was analyzed using X-ray diffraction (XRD) and Raman spectroscopy before and after annealing. Laser annealing was also conducted in-situ during Raman analysis with a 532 nm laser; spectra were collected at 1% power (0.45 mW) after annealing for 10 seconds each at increasingly higher power as detailed in Figure 2. Exposure times longer than 10 seconds did not correspond to any additional changes in material structure.

Characterization

X-Ray Diffraction. XRD was performed using a PANalytical Xpert Pro MPD with a Cu source, a theta-theta goniometer, parallel beam optics, line focus in reflection mode, with a PIXcel 1D detector operating from 20-80 2θ for a 15 minute scan using a multi-purpose stage.

Raman Spectroscopy. Raman spectroscopy was performed using a 532 nm laser with a maximum power at the sample of 45 mW (notch filter $\pm 10 \text{ cm}^{-1}$), a back illuminated detector (2048x512 pixel), a 100x objective (NA 0.9 WD 0.2 mm), and 300 g/mm grating (spectral resolution $\sim 4 \text{ cm}^{-1}$ @ 532 nm) using an input laser power range of 1% to 25% power.

Optical Profilometry. Profilometry was performed using a Zygo Nexview 3D profilometer with a 50x objective with a 2x internal multiplier. Auto-light settings were used to properly image topography, with an internal masking and calibration used to set baselines of the glass background.

Scanning Electron Microscopy (SEM) and Energy Dispersivity X-ray Spectroscopy (EDS). SEM images and EDS maps were taken on a FEI Nova NanoSEM 630 SEM with an accelerating voltage of 7 keV for imaging and 15 keV for EDS. Samples were coated with a 5 nm layer of iridium metal to prevent charge build-up.

Cross Sectioning. Cross sectioning was done by first cutting excess glass to expose the sample using a Leica EM TPX. Polishing was then done with a 9 μm diamond lapping foil to smooth the surface and prepare the sample for ion milling. The final ion milling was done with a Leica EM TIC 3X for 4 hrs at 8 kV.

Measurement of Thermal Conductivity. To measure the thermal conductivity of the direct-write structures, we deposited an 80 nm Al film on the microstructures via electron beam evaporation to perform time-domain thermoreflectance (TDTR) measurements; details of the specific TDTR system has been discussed in-depth in previous works²⁻³. In brief, TDTR is a pump-probe method in which a modulated laser pulse creates a heating event on the surface of a thin metal transducer. A second laser pulse, the probe beam, is temporally-delayed with a mechanical delay stage and interacts with the heated area; we measure the reflectivity of the probe beam as a function of delay time between the two pulses, thus obtaining a rate of thermal dissipation into the underlying substrate. This curve is then fit with a thermal model⁴ to obtain the thermal properties of the material system of interest.

The measured values for thermal conductivity as well as values for the volumetric heat capacity, as obtained in reference⁵ are shown in Table S3. We note that the sample surface is more rough than typical TDTR measurements and the underlying structure degrades at relatively low power densities, leading to higher error than typically found in TDTR experiments. Further, as we use fully-dense, bulk material values for the volumetric heat capacity in our thermal model, any changes in the sample density will lead to a change in the measured thermal conductivity. Nonetheless, the lack of trend between line-width and thermal conductivity of the direct write structure is quite clear.

The thermal conductivity of a crystalline Fe_2O_3 (hematite) was extrapolated to $6.4 \text{ W m}^{-1} \text{ K}^{-1}$ at room temperature, based on previously reported data⁶. As the deposited iron oxide in this work is known to be amorphous, a marked decrease in thermal conductivity would be expected. Literature values for the thermal conductivity of copper oxide are quite wide-spread and are recognized to be highly phase-dependent. For example, Cu_2O has a reported thermal conductivity of $\sim 5 \text{ W m}^{-1} \text{ K}^{-1}$,⁷ with *ab initio* calculations predicting even lower values⁸, whereas CuO has been assumed to have values as high of $69 \text{ W m}^{-1} \text{ K}^{-1}$ or as low as $20 \text{ W m}^{-1} \text{ K}^{-1}$.⁸⁻¹¹ It is quite possible that these variations are due to physical differences in measured samples, and thus contribute to the large error found in the measured thermal conductivity of CuO in this work. Similar issues in comparing our measured thermal conductivity values to reported literature values for Cr_2O_3 and Co_3O_4 , as both lack consistent values. For example, Hay *et al.* report a value of $\sim 5 \text{ W m}^{-1} \text{ K}^{-1}$ for Cr_2O_3 coatings¹², whereas Marinelli *et al.* measure a thermal conductivity of $\sim 13 \text{ W m}^{-1} \text{ K}^{-1}$ for bulk Cr_2O_3 at room temperature¹³.

Material	Line width (μm)	Laser power (mW)
Mn_2O_3	2.5	23
CuO	2.5	32
NiO	5.5	53
Cr_2O_3	8	37
Fe_2O_3	14.5	53
Co_3O_4	2.5	23
Pt	2.5	47

Table S1. Minimum line widths achieved for a range of materials using a 60x, 1.4 N.A. objective at the stated laser powers as measured at the back of the objective. Lines were deposited by rastering the laser using a galvoscaner in a 10 micron line at a rate of 5 passes/s. The stage was manually translated along the direction of the scan to induce material deposition. The galvo scanning was used in addition to the stage translation in order to promote bubble de-pinning at the leading edge of deposition. Laser power was modulated to find minimum achievable line widths. Precursors used were the same as given in Table 1.

Material	Line Width (μm)
Cr ₂ O ₃	8.1
Mn ₂ O ₃	8.1
CuO	2.5
NiO	5.4
Co ₃ O ₄	8.3
Fe ₂ O ₃	14.5

Table S2. Line widths for a range of materials deposited under the same laser deposition conditions. Materials were deposited by rastering the laser in a 10 micron line at rate of 5 passes/s and manually translating the stage in the direction of the scan. All samples deposited using a 60x, N.A. 1.4 objective at a power of 53 mW as measured at the back of the objective. Precursors used were the same as given in Table 1.

Material	Specific Heat ($\text{cal g}^{-1} \text{K}^{-1}$)	Density (g cm^{-3})	Thermal Conductivity ($\text{W m}^{-1} \text{K}^{-1}$)	Error in Thermal Conductivity
Co ₃ O ₄	0.125	6.11	0.8	0.3
CuO	0.125	6.31	26.6	10
Cr ₂ O ₃	0.175	5.22	1.54	0.5
Fe ₂ O ₃	0.15	5.24	1.7407	0.5

Table S3. Data for volumetric heat capacity (from reference⁵) and measured thermal conductivity of selected oxides. We do not observe correlation of thermal conductivity with minimum line width trends.

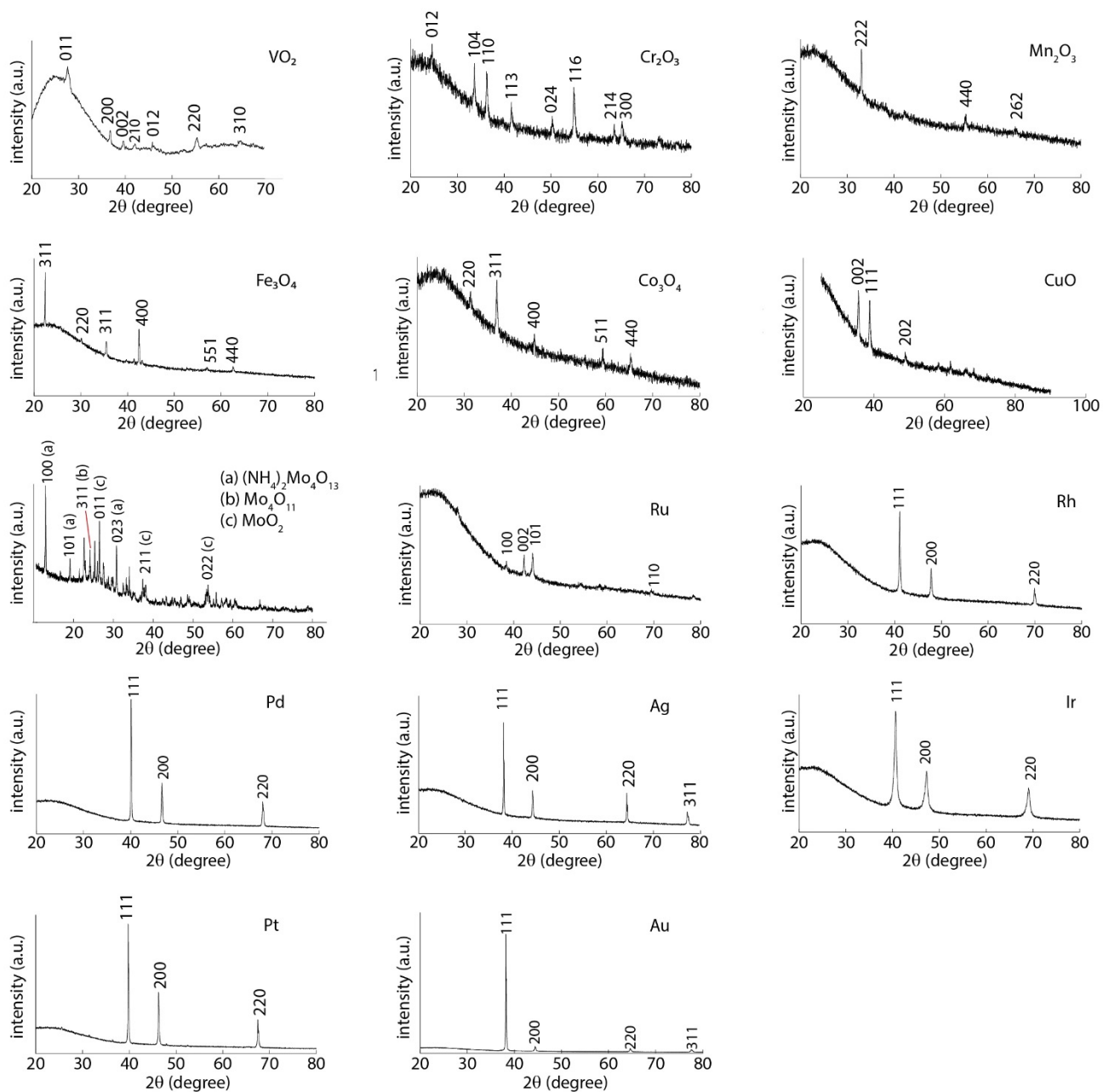


Figure S1. XRD data used to identify compounds listed in Table 1 in the main text.

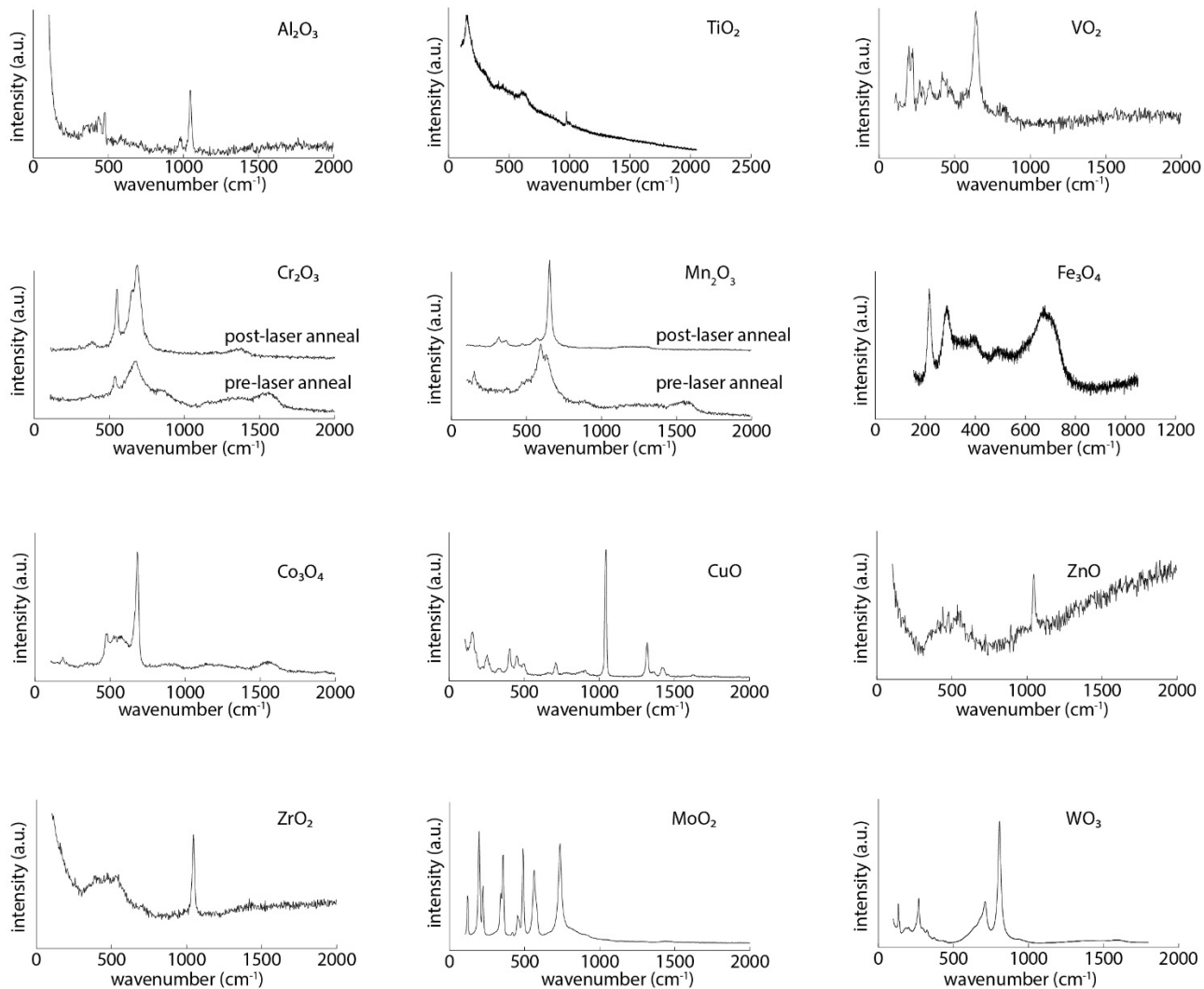


Figure S2. Raman spectroscopy data used for identification of compounds listed in Table 1 of the main text. For the Cr_2O_3 and Mn_2O_3 in-situ laser annealing during Raman analysis using the 532 nm laser was conducted, similar to the experiment described in Figure 2, and the pre- and post-anneal spectra are given for comparison.

References

1. Zarzar, L. D.; Swartzentruber, B. S.; Donovan, B. F.; Hopkins, P. E.; Kaehr, B., Using laser-induced thermal voxels to pattern diverse materials at the solid–liquid interface. *ACS Applied Materials & Interfaces* **2016**, *8* (33), 21134-21139.
2. Hopkins, P. E.; Duda, J. C.; Kaehr, B.; Wang Zhou, X.; Peter Yang, C.-Y.; Jones, R. E., Ultrafast and steady-state laser heating effects on electron relaxation and phonon coupling mechanisms in thin gold films. *Applied Physics Letters* **2013**, *103* (21), 211910.
3. Hopkins, P. E.; Serrano, J. R.; Phinney, L. M.; Kearney, S. P.; Grasser, T. W.; Harris, C. T., Criteria for Cross-Plane Dominated Thermal Transport in Multilayer Thin Film Systems During Modulated Laser Heating. *Journal of Heat Transfer* **2010**, *132* (8), 081302-081302-10.
4. Cahill, D. G., *Review of Scientific Instruments* **2004**, *75* (12), 5119-5122.
5. Touloukian, Y.; Buyco, E., Specific Heat: Nonmetallic Solids, Vol. 5. *Thermophysical Properties of Matter* **1970**, 19702, 24.

6. Molgaard, J.; Smeltzer, W., Thermal conductivity of magnetite and hematite. *Journal of Applied Physics* **1971**, *42* (9), 3644-3647.
7. Lide, D. R., *CRC handbook of chemistry and physics*. CRC press: **2004**; Vol. 85.
8. Linnera, J.; Karttunen, A., Ab initio study of the lattice thermal conductivity of Cu₂O using the generalized gradient approximation and hybrid density functional methods. *Physical Review B* **2017**, *96* (1), 014304.
9. Liu, M. S.; Lin, M. C.; Huang, I. T.; Wang, C. C., Enhancement of thermal conductivity with CuO for nanofluids. *Chemical Engineering & Technology: Industrial Chemistry-Plant Equipment-Process Engineering-Biotechnology* **2006**, *29* (1), 72-77.
10. Xue, Q.; Xu, W.-M., A model of thermal conductivity of nanofluids with interfacial shells. *Materials Chemistry and Physics* **2005**, *90* (2-3), 298-301.
11. Kusiak, A.; Battaglia, J.-L.; Gomez, S.; Manaud, J.-P.; Lepetitcorps, Y., CuO thin films thermal conductivity and interfacial thermal resistance estimation. *The European Physical Journal-Applied Physics* **2006**, *35* (1), 17-27.
12. Hay, B.; Davee, G.; Filtz, J.-R.; Hameury, J.; Rongione, L., *Thermal Conductivity 30: Thermal Expansion 18: Joint Conferences* **2009**, 461.
13. Marinelli, M.; Mercuri, F.; Zammit, U.; Pizzoferrato, R.; Scudieri, F.; Dadarlat, D., Critical behavior of thermal diffusivity and thermal conductivity of Cr₂O₃ at the Neel transition. *Physical Review B* **1994**, *49* (6), 4356-4359.